

Fireballs, Flares and Flickering: A Semi-analytic, LTE, Explosive Model from Accretion Disks to Supernovae

K. J. Pearson

Louisiana State University, Department of Physics and Astronomy, Nicholson Hall, Baton Rouge, LA 70803-4001

Keith Horne

School of Physics and Astronomy, University of St. Andrews, North Haugh, St. Andrews KY16 9SS
and

Warren Skidmore

Caltech, Mail code 105-24, Pasadena, CA 91125-24

ABSTRACT

We derive simple analytic expressions for the continuum lightcurves and spectra of flaring and flickering events that occur over a wide range of astrophysical systems. We compare these results to data taken from the cataclysmic variable SS Cygni and also with SN 1987A, deriving physical parameters for the material involved. Fits to the data indicate a nearly time-independent photospheric temperature arising from the strong temperature dependence of opacity when hydrogen is partially ionized.

Subject headings: accretion, accretion disks - binaries:close - novae: cataclysmic variables - radiative transfer - stars: individual: SS Cygni - supernovae: individual: SN 1987A

1. Introduction

In a recent paper (Pearson, Horne & Skidmore 2003), we explained the unusual flaring activity of the cataclysmic variable (CV) system AE Aqr in terms of the aftermath of the collision between two gas clouds. We modelled the resulting fireball numerically, comparing the results to analytic approximations for the optical lightcurves and continuum spectra and to observed lightcurves and spectra. We set out here an improved analytic calculation for an expanding fireball with an LTE ionization structure and compare our results to more detailed numerical simulations. We fit our results to multiwavelength lightcurves of two very different systems; deriving values for the physical conditions in them.

Flickering and flaring occurs across the whole range of astrophysical systems from stars to active

galaxies. It appears to be a recurrent feature of accreting systems and, in particular, those where an accretion disk is present. This flickering process may well be associated with the anomalously high viscosity present in these systems and represent the effect of magnetic reconnections such as that from the viscosity mechanisms of Hawley & Balbus (1991). Such a sudden localised deposition of energy would raise the gas temperature and the consequent overpressure would give rise to a local expansion of the disk material. With material cooling adiabatically, this expansion would rapidly become supersonic.

Observations by Bruch (2000) suggest that the flickering in CVs is not uniformly distributed across the disk but instead is associated with the stream-disk impact point and the innermost boundary layer region of the disk. Similarly Pat-

terson (1981) found that the flickering in HT Cas was associated with the inner part of the accretion disk. These findings, however, are contradicted by Welsh & Wood (1995) for HT Cas, by Baptista (2004) for V2051 Oph and Baptista (2002) for the Low-Mass X-ray Binary (LMXB) X1822-371. All these studies show flickering to arise from a range of disk radii.

The terms “flickering” and “flaring” are often used interchangeably when describing the stochastic variability of accreting sources and, even when defined in a particular field, are not necessarily used consistently. Warner (1995) and Baptista (2004) describe flickering in CVs as the continuous, random brightness fluctuations of 0.01–1 mag on timescales of seconds to dozens of minutes although the exact numerical ranges differ between the two. In contrast the unusual CV AE Aqr is universally described as a “flaring” source since it has rarer by brighter events that often occur in batches. These events can raise the total optical luminosity of the system by factors of 2-3 contrasting with the 5-20% typical of CV flickering (Bruch 1992) but on a similar timescale. Consequently, we adopt the convention of describing the small amplitude, continuous variations as “flickering” and reserve the term “flaring” for larger scale events.

The underlying model used to reproduce the AE Aqr lightcurves was based on consideration of the flux emitted by a hot, spherically symmetric ball of gas as it expanded and cooled. While we saw that the “expanding fireball” situation in AE Aqr could arise from collisional heating of gas blobs, the same situation might arise from the very different causes outlined above. As a result, these “fireball” models may have a much wider range of applicability than simply the unusual behaviour of AE Aqr. Accordingly, in this paper, we will compare analytic expressions derived for the lightcurves of such expansions to observations of SS Cygni and SN 1987A.

SS Cyg is a member of the dwarf nova subclass of cataclysmic variables. It consists of a $1.2M_{\odot}$ white dwarf accreting material through an accretion disk from a $0.71M_{\odot}$ K5V secondary that loses material via Roche lobe overflow (Ritter & Kolb 2003). SS Cyg was the second member of this subclass identified (Wells 1896) and has had a near continuously monitored lightcurve for over a century (Warner 1995). Like all dwarf novae,

SS Cyg exhibits optical variability over a large range of timescales e.g. outbursts ($\Delta m \approx 3.5$ mag, $t \approx 40$ days), orbital modulations ($\Delta m \approx 0.5$ mag, $P = 0.275130$ days), flickering ($\Delta m = 0.01 - 0.2$ mag, $t \sim 1$ min) and Dwarf Nova Oscillations ($\Delta m \approx 0.02$ mag, $t \approx 2.8 - 10.9$ s) (Mauche & Robinson 2001; van Teeseling 1997; Honey et al. 1989; Warner 1995, 2004). We shall concentrate our modelling on the lightcurve from a flickering event.

SN 1987A was the brightest supernova observed since Kepler’s in 1604. The lightcurve can be broken into three phases: a “flash” lasting a few hours, a subsequent “bump” lasting around 4 months and a final exponential “tail” powered by radioactive decay of unstable nuclei in the ejecta. It was a type II supernova with an identified progenitor (Sk-69°202) that was a blue supergiant. It is believed that it lasted $\sim 10^7$ y as a 20-30 M_{\odot} main sequence blue supergiant star, before becoming a red supergiant for $\sim 10^6$ y during which phase it lost 3-6 M_{\odot} before finally becoming a blue supergiant again for a few thousand years (McCray 1993). The rebrightening “bump” phases arises from a photosphere moving out with expelled material and eventually reversing as the material becomes optically thin again. It is interesting to note that the photosphere maintained a roughly constant temperature ~ 6000 K close to the recombination temperature for hydrogen at the expected densities in the expanding shell. The models of AE Aqr flares in Pearson, Horne & Skidmore (2003) showed a similar isothermal behaviour.

2. Model Assumptions

We briefly recap here the dynamical model developed in Pearson, Horne & Skidmore (2003) but the interested reader is referred there for a more detailed derivation. Let us assume a spherically symmetric expansion of a Gaussian density profile with radial velocity proportional to the distance from the centre of the expansion. We define

$$\eta \equiv \frac{r}{a} \quad (1)$$

as a dimensionless measure of the radius r in terms of the current lengthscale of the Gaussian a . The expansion factor β acts as a dimensionless time, being the constant of proportionality between the

current and fiducial scalelength a_0 . Hence,

$$\beta \equiv \frac{a}{a_0} \quad (2)$$

consistent with our above assumptions regarding velocity and implying

$$\beta = 1 + H (t - t_0) \quad (3)$$

where t_0 is the time at which all the fiducial values are determined and H is an ‘‘expansion constant’’ setting the speed of the expansion. For simplicity, we consider only the case of uniform 3-D expansion, avoiding factors such as the angle of the observer to lines of symmetry. We also restrict ourselves to a spatially uniform temperature distribution since, for example, a power law distribution gives a result for the later integration in (22) in terms of the hypergeometric function ${}_2F_1$. We assume a power law with index Γ for the temporal dependance of temperature. $\Gamma = 0$ corresponds to an isothermal expansion and $\Gamma = 2$ to the adiabatic case.

In summary then, we have

$$T = T_0 \beta^{-\Gamma}, \quad (4)$$

$$\rho = \rho_0 \beta^{-3} e^{-\eta^2}, \quad (5)$$

where

$$\rho_0 = \frac{M}{(\pi a_0^2)^{\frac{3}{2}}} \quad (6)$$

and M is the total mass involved in the expansion.

Using $v(r) = Hr_0 = Hr\beta^{-1}$ we can integrate $\frac{1}{2}\rho v^2$ over all space to derive the total kinetic energy of the expansion

$$E_{\text{kin}} = \frac{2}{\sqrt{\pi}} M a_0^2 H^2 \int_0^\infty \eta^4 e^{-\eta^2} d\eta \quad (7)$$

$$= \frac{3}{4} M a_0^2 H^2 \quad (8)$$

$$\equiv \frac{3}{4} M v_0^2 \quad (9)$$

defining $v_0 = Ha_0$, the speed of expansion at $r = a$.

3. Theoretical Lightcurves and Spectral Distributions

The radiative transfer equation has a formal solution under conditions of LTE

$$I = \int_0^\infty B e^{-\tau} d\tau, \quad (10)$$

where I is the intensity of the emerging radiation, B is the Planck function and τ is the optical depth measured along the line of sight from the observer. For cases where the source function is everywhere the same this becomes

$$I = B (1 - e^{-\tau}). \quad (11)$$

We define x as the distance from the fireball centre toward the observer, and y as the distance perpendicular to the line of sight. The above line integral (equation (11)) gives the intensity $I(y)$ for lines of sight with different impact parameters y . The fireball flux, obtained by summing intensities weighted by the solid angles of annuli on the sky, is then

$$f(\lambda) = \int_0^\infty I(y) \frac{2\pi y}{d^2} dy \quad (12)$$

where d is the source distance.

We can calculate the evolution of the continuum lightcurve using expressions for the linear absorption coefficient. The free-free absorption coefficient (per unit distance) can be written as

$$\kappa_{\text{ff}} = \kappa_0 \left[1 - e^{-\left(\frac{h\nu}{kT}\right)} \right] T^{-\frac{1}{2}} \nu^{-3} n_e n_i \quad (13)$$

where

$$\kappa_0 = 3.692 \times 10^{-2} Q^2 g_{\text{ff}} \text{ (SI)} \quad (14)$$

(Keady & Kilcrease 2000), g_{ff} is the free-free Gaunt factor (Gaunt 1930) and Q the ionic charge. We wish to retain the explicit frequency dependence but otherwise follow a parallel derivation as for Kramers’ opacity. For a mixed elemental composition, then, we sum over all species (assumed fully ionized)

$$\sum_{\text{all ions}} Q_i^2 n_i g_{i,\text{ff}} \approx \frac{\rho}{m_{\text{H}}} (1 - Z) \bar{g}_{\text{ff}} \quad (15)$$

(Bowers & Deeming 1984). Here \bar{g}_{ff} is a mean Gaunt factor (close to unity) and Z the metal mass fraction. We also have

$$n_e = \frac{\rho}{\mu_e m_{\text{H}}} = \frac{\rho (1 + X)}{2 m_{\text{H}}} \quad (16)$$

(Bowers & Deeming 1984) where X is the hydrogen mass fraction. Combining and writing the correction for stimulated emission as

$$\epsilon = 1 - e^{-\left(\frac{h\nu}{kT}\right)} \quad (17)$$

gives

$$\kappa_{\text{ff}} = \kappa_1 \epsilon \rho^2 T^{-\frac{1}{2}} \nu^{-3} \quad (18)$$

where we have defined

$$\kappa_1 = 6.695 \times 10^{51} (1 - Z) (1 + X) \bar{g}_{\text{ff}} \text{ (SI)}. \quad (19)$$

Inserting our density profile (equation (5)) we arrive at the result

$$\kappa_{\text{ff}} = \frac{\kappa_1 \epsilon}{T^{\frac{1}{2}} \nu^3 \pi^3 a^6} M^2 e^{-2\eta^2}. \quad (20)$$

On dimensional grounds if on no other, a similar expression to equation (18) and hence (20) must also exist for bound-free opacity when it dominates (when most species are fully recombined). Textbook derivations of Kramer's opacity (eg. Bowers & Deeming 1984) show us

$$\kappa_{1,\text{bf}} \propto Z (1 + X) \bar{g}_{\text{bf}} \quad (21)$$

where g_{bf} is the bound-free Gaunt factor (Gaunt 1930). Useful tables for g_{bf} have been calculated by Glasco & Zirin (1964). The constant of proportionality, however, is more difficult to determine than for free-free, since it must account for the ionization edges in the absorption and, in particular, the change of energy level populations with temperature for each ion. We shall assume a relation analogous to equation (18) also holds for the situation of mixed ionized and recombined species where both forms of opacity contribute.

The optical depth parallel to the observers line of sight

$$\tau(y) = - \int_{\infty}^{-\infty} \kappa \, dx \quad (22)$$

$$= \left[\frac{\kappa_1 \epsilon}{T^{\frac{1}{2}} \nu^3 \pi^3 a^5} \right] e^{-2(\frac{y}{a})^2} \int_{-\infty}^{\infty} e^{-2(\frac{x}{a})^2} d\left(\frac{x}{a}\right) \quad (23)$$

$$= \tau_0 e^{-2(\frac{y}{a})^2} \quad (24)$$

where the optical depth on the line of sight through the centre of the fireball is

$$\tau_0 = \left(\frac{\beta_c}{\beta} \right)^{\left(\frac{10-\Gamma}{2} \right)} \quad (25)$$

and the time at which the fireball becomes optically thin along this line of sight is

$$\beta_c \equiv \left[\frac{\kappa_1 \epsilon}{T_0^{\frac{1}{2}} \nu^3 \sqrt{2} \pi^5 a_0^5} \right]^{\frac{2}{10-\Gamma}}. \quad (26)$$

It should be noted that in pulling $\kappa_1(\mu_i, \mu_e)$ out of the integral (23) we have implicitly assumed that the spatial variation of the ionization fraction has negligible impact on the behaviour. This is an assumption that we shall return to later.

In Pearson, Horne & Skidmore (2003) we approximated the flux received from the fireball by splitting it into two components as viewed on the plane of the sky: an optically thick central region bounded by $y = y_m$ (see equation 44) and an optically thin surrounding. Here, however, we calculate the integral exactly. Combining equations (11), (12) and (24) with a change of integration variable to $u = \tau(y)$, we have

$$f = \frac{\pi a^2 B}{2 d^2} \int_0^{\tau_0} \frac{1 - e^{-u}}{u} du \quad (27)$$

Expressing the exponential in its series form we integrate to find

$$f = \frac{\pi a^2 B}{2 d^2} \sum_{n=1}^{\infty} \frac{(-1)^{(n+1)} \tau_0^n}{n n!} \quad (28)$$

which can also be rewritten in the form of standard functions

$$f = \frac{\pi a^2 B}{2 d^2} (E_1(\tau_0) + \gamma + \ln(\tau_0)) \quad (29)$$

where E_1 is the first order exponential integral and $\gamma \approx 0.577216$ is Euler's gamma constant (Abramowitz & Stegun 1972; Jeffreys & Jeffreys 1956; Press et al. 1992). This has the form of

$$f = \Omega B S(\tau_0), \quad (30)$$

where $\Omega = \frac{\pi a^2}{2 d^2}$ is the solid angle subtended by the current standard deviation ($a/\sqrt{2}$) of the Gaussian density profile and the "Saturation Function"

$$S(\tau_0) = (E_1(\tau_0) + \gamma + \ln(\tau_0)) \quad (31)$$

is plotted in Figure 1. We note the asymptotic limits

$$S(\tau) \approx \begin{cases} \tau & \text{for } \tau \ll 1 \\ \gamma + \ln \tau & \text{for } \tau \gg 1. \end{cases} \quad (32)$$

The intensity of emitted radiation as a function of impact parameter is plotted for different times in Figure 2. We can see how the flux saturates at the black body function for highly optically thick

impact parameters. In comoving coordinates this region gradually shrinks and at later times the entire emission becomes optically thin.

The total flux given by equation (29) is plotted against time in Figure 3 for different values of Γ , using $\beta_c = 1$. Figure 4 shows lightcurves at different wavelengths assuming $\Gamma = 0$ (isothermal) and $\beta_c = (\lambda/5000 \text{ \AA})^{\frac{3}{5}}$. The effect of the expanding photosphere can be seen from the optically thick contribution to the total flux, the latter of which rises to a peak at β_{pk} . Initially the optically thick flux is the dominant source and the emission rises as the emitting area grows while the photosphere is advected outwards. Eventually, the decreasing density causes the photosphere to reverse and begin to shrink, reaching zero size at $\beta = \beta_c$. The remaining emission comes from the optically thin region surrounding the optically thick circle as seen on the plane of the sky. This optically thin emission dominates at late times.

Recalling that $a = \beta a_0$, for the special case of $\Gamma = 0$ (isothermal expansion) we can neglect the time variation of the Planck function and differentiate (29) with respect to β to find a condition for the maximum flux

$$4(E_1(\tau_0) + \gamma + \ln(\tau_0)) - (10 - \Gamma)(1 - e^{-\tau_0}) = 0. \quad (33)$$

This can be solved numerically to find $\tau_{0,\text{pk}} = 6.8204$. From (25) we then find $\beta_{\text{pk}} = 0.6811\beta_c$. We can also differentiate (29) with respect to β for $\Gamma \neq 0$ although the form is much more untidy and we must solve for β directly. We plot β_{pk} against Γ in Figure 5 continuing to neglect any time de-

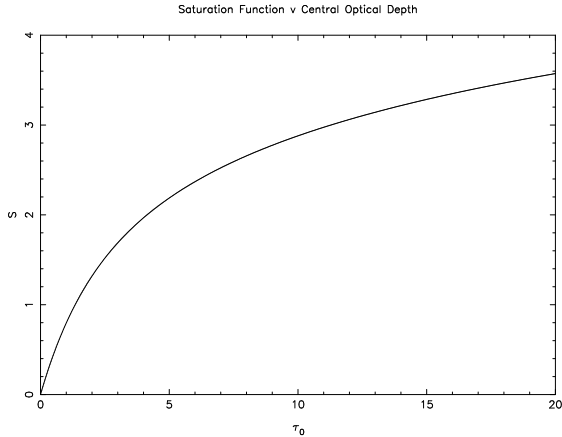


Fig. 1.— The Saturation Function S .

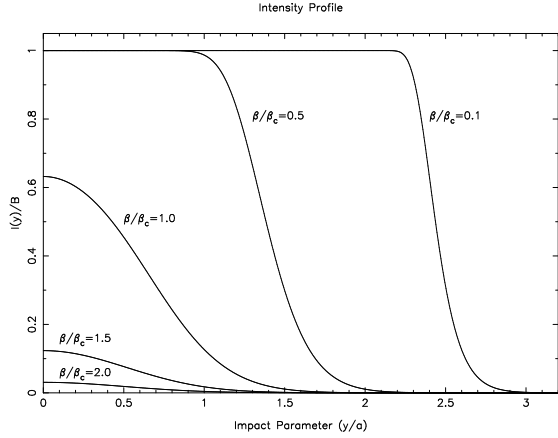


Fig. 2.— Comparison of the intensity profiles at different times calculated using (24) and (11) for a $\Gamma = 0$ (isothermal) evolution.

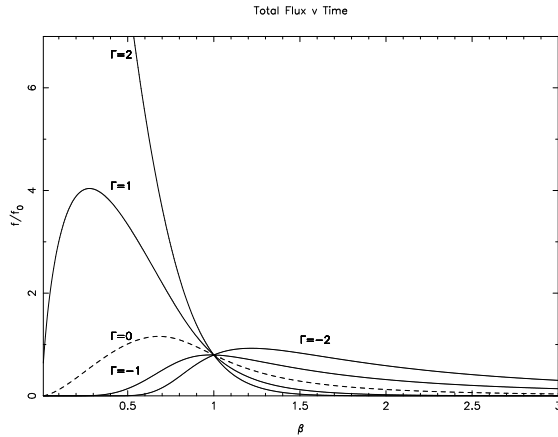


Fig. 3.— The temporal behaviour of the total flux at 5000 \AA for different cooling indices $\Gamma = -2, -1, 0, 1, 2$, assuming $\beta_c = 1$ and $T_0 = 15\,000 \text{ K}$. The y-axis is parameterised in multiples of $f_0 = \frac{\pi a_0}{2d^2} B_\nu(5000 \text{ \AA}, 15\,000 \text{ K})$.

pendence of ϵ . We plot β_{pk} against wavelength in Figure 6 for several values of Γ .

Bruch (1992) found a correlation between the amplitude of flickering in different wavebands for several CVs (see *inter alia* his Figure 2). Such a correlation could arise from an isothermal evolution at a consistent temperature. This can be understood from (29). Since the peak flux occurs at the same central optical depth independent of wavelength, then for two wavelengths λ_1 and λ_2 the peak fluxes are related by

$$\frac{f_{\text{pk},1}}{f_{\text{pk},2}} = \left(\frac{\beta_{\text{pk},1}}{\beta_{\text{pk},2}} \right)^2 \frac{B_{\lambda,1}}{B_{\lambda,2}} \quad (34)$$

$$= \left(\frac{\beta_{c,1}}{\beta_{c,2}} \right)^2 \left(\frac{\lambda_1}{\lambda_2} \right)^{-5} \left(\frac{e^{\frac{c_2}{\lambda_2 T_0}} - 1}{e^{\frac{c_2}{\lambda_1 T_0}} - 1} \right) \quad (35)$$

$$= \left(\frac{\lambda_2}{\lambda_1} \right)^{\frac{19}{5}} \left(\frac{1 - e^{-\frac{c_2}{\lambda_1 T_0}}}{1 - e^{-\frac{c_2}{\lambda_2 T_0}}} \right)^{\frac{2}{5}} \left(\frac{e^{\frac{c_2}{\lambda_2 T_0}} - 1}{e^{\frac{c_2}{\lambda_1 T_0}} - 1} \right) \quad (36)$$

where $c_2 = hc/k$ and assuming no complications such as a Balmer edge between them. We plot the predicted values for different temperatures as stars; alongside the data taken from Table 4 of Bruch (1992), in a color-color diagram in Figure 7 (nb. we used B_λ rather than B_ν in the above derivation purely for comparison with this dataset).

This figure shows that a simple application of our model enables us to reproduce the observed range of V-B reasonably well using T as a free parameter. The U-B colour however, is generally underpredicted. This results from not making allowance for the increased opacity above the Balmer jump when evaluating β_c in deriving 36. The size of the Balmer jump depends upon a non-trivial combination of mass, lengthscale and temperature to produce an effective value of κ_1 . Any individual system may produce flickers with a range of physical parameters causing it to produce points scattered across this diagram.

Using numerical methods outlined later, we derived values for κ_1 for several temperatures over a range of densities. These are plotted in Figure 8. We can see how, for a large range of temperatures of interest and for densities ranging over several orders of magnitude, κ_1 is well represented by a constant value. At lower temperatures the free-free

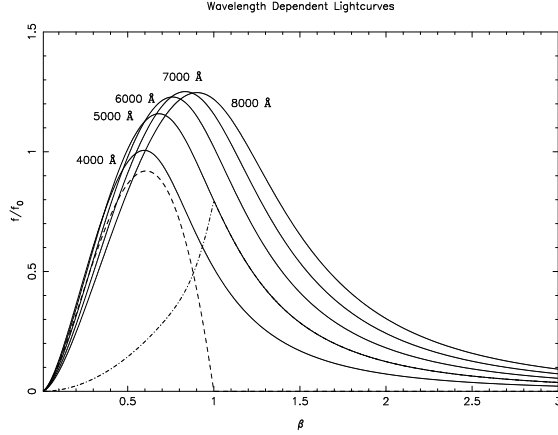


Fig. 4.— The temporal behaviour of the total flux at several wavelengths assuming $\beta_c = \left(\frac{\lambda}{5000 \text{ \AA}} \right)^{\frac{3}{5}}$, $T_0 = 15\,000 \text{ K}$ and $\Gamma = 0$. The y-axis is again parameterised in multiples of f_0 . The optically thick contribution at 5000 \AA is plotted as a dashed line and the optically thin contribution as a dot-dashed line.

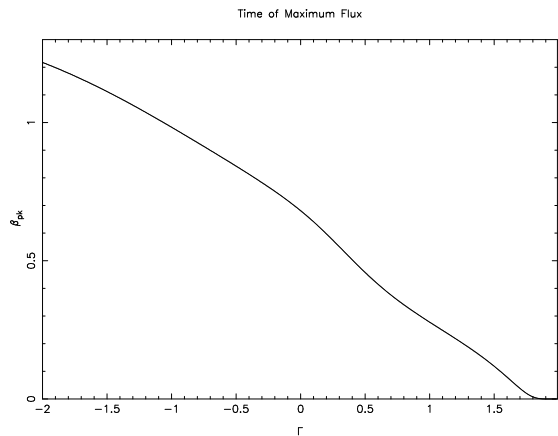


Fig. 5.— The time of peak flux at 5000 \AA plotted against Γ , assuming $\beta_c = 1$ and $T_0 = 15\,000 \text{ K}$.

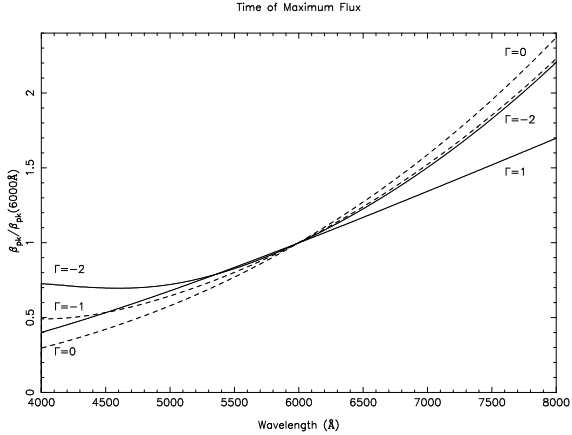


Fig. 6.— The time of peak flux plotted against wavelength for various values of Γ assuming $T_0 = 15\,000$ K. The values are normalised to the peak time at 6000 \AA in each case.

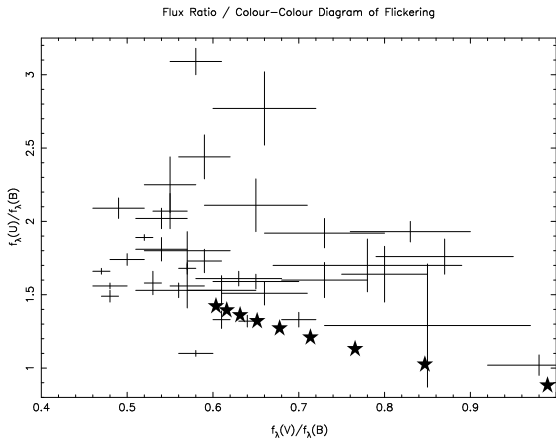


Fig. 7.— The amplitude ratio (a U-B v V-B color-color diagram) for flickering in several CVs observed by Bruch (1992). The predicted values are plotted as stars for different temperatures ranging from 8000 K (extreme right) to $24\,000$ K in 2000 K steps.

opacity transitions to bound-free opacity at lower densities than it does at higher temperatures. At these lower temperatures we could introduce significant errors if we estimate κ_1 from a position that has one form of opacity when the other is in fact dominant. It is very unlikely that this would be the case, however, if we estimate the ionization state from conditions at a suitable position and consider how κ_1 smoothly changes with the ionization. Qualitatively then, at the very least, we can be confident of the ability of the analysis to allow us to examine the behaviour of the proposed mechanism and to predict fluxes to within factors of order unity.

4. Analysis

Equation (29) gives us the complete temporal and frequency behaviour for the emergent flux in terms of τ_0 . We must use the Planck function appropriate to the time-dependent behaviour of the temperature from (4). Equation (25) gives us τ_0 as a function of β and β_c . The behaviour of the flux thus rests on the character of the parameter β_c . We know functionally that

$$\beta_c = \beta_c(\kappa_1, \epsilon, \nu^{-3}), \quad (37)$$

$$\kappa_1 = \kappa_1(\eta, \nu, \beta), \quad (38)$$

$$\epsilon = \epsilon(\nu, \beta) \quad (39)$$

and we shall examine each of these dependencies and appropriate levels of approximation in each case.

4.1. Global Behaviour $\beta_c = \text{const}$

In examining the behaviour of the flux as a function of time it is instructive to restrict ourselves initially to a single wavelength and ignore spatial or time dependency in β_c .

We see from equations (25) and (28) that the late-time behaviour ($kT \ll h\nu$) of the lightcurve is determined by the temperature index Γ such that $f \sim \beta^{-5}$ or β^{-4} for isothermal or adiabatic cooling respectively.

4.2. Spatial Dependence $\beta_c = \beta_c(\eta)$

4.2.1. One Zone Model

We know β_c depends on κ_1 which in turn depends on the ionization structure across the ex-

pansion. At the outset we acknowledge that a detailed solution accounting for the changing ionization fraction across the density profile would require numerical integration such as that reported in Pearson, Horne & Skidmore (2003) for AE Aqr. We are looking for simpler, more easily calculable approximations that avoid such detailed methods. To this end we do not include here any explicit allowance for the variation of ionization states across the profile; instead we approximate the behaviour by calculating the conditions at a suitable point within the expansion. With a Gaussian density profile we might expect the flux to be dominated by the region close to the photosphere. As a result we could approximate the ionization structure by the solution to the Saha equation under the conditions prevailing there.

To find the position of the observed photosphere we need to integrate along a given line of sight until optical depth unity. From our earlier derivation we can see the optical depth down to any height x' is

$$\tau(y) = \tau_0 \frac{\sqrt{2}}{\sqrt{\pi}} e^{-2(\frac{y}{a})^2} \int_{\frac{x'}{a}}^{\infty} e^{-2(\frac{x}{a})^2} d\left(\frac{x}{a}\right) \quad (40)$$

which, setting $\tau(y) = 1$ for the special case $x' = x_{\text{ph}}$ gives

$$e^{2(\frac{y}{a})^2} = \frac{1}{2} \tau_0 \operatorname{erfc}\left(\sqrt{2} \frac{x_{\text{ph}}}{a}\right). \quad (41)$$

This defines the locus of points on the photospheric surface. Since the largest contribution to the opacity integral comes from the region of highest density, we will introduce least error by evaluating κ_1 there. This will clearly occur along the central line of sight $y = 0$ and hence we arrive at

$$\operatorname{erfc}(\sqrt{2}\eta_{\text{ph}}) = \frac{2}{\tau_0} \quad (42)$$

which we must solve numerically. However, we must remember that it is possible for the photospheric surface to lie behind the density peak. This will just occur when $\tau(0) = 1$ at $\eta = 0$, implying $\beta = 2^{(\frac{2}{10-\Gamma})} \beta_c$. Ultimately then, we have

$$\rho_{\text{eval}} = \begin{cases} \rho_0 \beta^{-3} e^{-\eta_{\text{ph}}^2} & \text{for } \beta < 2^{(\frac{2}{10-\Gamma})} \beta_c \\ \rho_0 \beta^{-3} & \text{otherwise.} \end{cases} \quad (43)$$

It must be emphasized that we are using this position solely to evaluate a typical ionization

state and, hence, to find a suitable approximate value for κ_1 . The effect of the density profile on the optical depth is accounted for explicitly in the derivations in section 3.

However, an alternative ‘typical’ place to estimate κ_1 is at the point of maximum density ($x = 0$) along the limiting impact parameter y_m that remains optically thick. We can derive y_m by setting (24) equal to unity, giving

$$y_m = a_0 \beta \left(\frac{\ln \tau_0}{2}\right)^{\frac{1}{2}} \quad (44)$$

where $\tau_0 > 1$ ie. for times $\beta < \beta_c$. Hence,

$$\rho_{\text{eval}} = \begin{cases} \rho_0 \beta^{\frac{(-2-\Gamma)}{4}} \beta_c^{\frac{(10-\Gamma)}{4}} & \text{for } \beta < \beta_c \\ \rho_0 \beta^{-3} & \text{otherwise.} \end{cases} \quad (45)$$

4.2.2. Pure hydrogen case - semi-analytic solution

For simplicity, let us consider a fireball with almost pure hydrogen composition (nb. if $Z = 0$ then equation (21) implies $\kappa_{1,\text{bf}} = 0$), with an ionization fraction

$$\iota \equiv \frac{n_i}{n_i + n_n} = \frac{n_i}{n}. \quad (46)$$

Ignoring any contribution to opacity from H^- and noting $\kappa \propto \rho^2$, the total opacity coefficient becomes

$$\kappa_1 \approx \iota^2 \kappa_{1,\text{ff}} + (1 - \iota)^2 \kappa_{1,\text{bf}}. \quad (47)$$

For hydrogen, the Saha equation can be approximated by

$$\frac{n_i n_e}{n_n} \approx 2.4 \times 10^{21} T^{\frac{3}{2}} \exp(-1.58 \times 10^5 T^{-1}) \text{ m}^{-3} \quad (48)$$

$$\frac{n_i^2}{n - n_i} = A(T) \quad (49)$$

(Lang 1980) where we have tidied the RHS into the function $A(T)$. Hence, we derive the quadratic

$$n_i^2 + A(T) n_i - A(T) n = 0 \quad (50)$$

and by restricting ourselves to the positive root arrive at

$$\iota = \frac{A}{2n} \left(\sqrt{1 + \frac{4n}{A}} - 1 \right). \quad (51)$$

We see then that the ionization fraction ι and parameter β_c are interdependent and should be solved for iteratively to ensure consistency. Thus we can determine the lightcurve behaviour by initially calculating a value for β_c from (26) with a judiciously chosen value for κ_1 . Thereafter we use the number density from (43) to calculate the ionization fraction from (51). This then allows us to find κ_1 from (47) and hence β_c again from (26) to better accuracy. We can repeat this iteratively to achieve the desired accuracy. This value can then be used to calculate the lightcurve behaviour at a given wavelength.

4.2.3. Mixed composition

For the more realistic case of mixed composition, we cannot calculate the ionization state at a given position analytically. Instead we must iteratively solve the network of Saha equations under the prevailing physical conditions to enable us to determine κ_1 . This solution can then iterated with β_c around the equations (26), (43) and κ_1 loop in a similar way to the above.

4.2.4. Three Zone Model

The above method works well in situations where either free-free or bound-free opacity is dominating. Unfortunately, as we noted at the end of section 3, in the situation of mixed opacity sources we can introduce significant errors if we use a value for κ_1 assuming the incorrect source. We can rescue much of the above formalism, however, if we split the spatial profile into 3 zones. We are almost bound to improve our calculation regardless of where we place the boundaries of the zones but clearly it makes sense to try to ensure that we have free-free dominated (outer regions), bound-free dominated (inner regions) and mixed (intermediate regions) zones. Assuming that hydrogen species provide the dominant opacity source, we select the boundary between these regions by the hydrogen ionization fractions $\iota = 0.1$ and $\iota = 0.9$ which occur at $\eta_{0.1}$ and $\eta_{0.9}$.

Specifically then, we need to replace the integral in equation (23) with one over the three types of zone and rework equation (26) to redefine β_c . Calculating $x_{0.1}$ and $x_{0.9}$ using $y = 0$ or y_m as

desired, the integral in (23) thus becomes

$$\begin{aligned} & \int_{-\infty}^{\infty} \kappa_1 e^{-2\left(\frac{x}{a}\right)^2} d\left(\frac{x}{a}\right) \\ &= \frac{2}{a} \int_0^{x_{0.1}} \kappa_{1,\text{bf}} e^{-2\left(\frac{x}{a}\right)^2} dx + \frac{2}{a} \int_{x_{0.1}}^{x_{0.9}} \kappa_{1,\text{m}} e^{-2\left(\frac{x}{a}\right)^2} dx \\ &+ \frac{2}{a} \int_{x_{0.9}}^{\infty} \kappa_{1,\text{ff}} e^{-2\left(\frac{x}{a}\right)^2} dx \end{aligned} \quad (52)$$

$$\begin{aligned} &= 2\kappa_{1,\text{ff}} \operatorname{erfc}\left(\sqrt{2}\frac{x_{0.9}}{a}\right) \\ &+ 2\kappa_{1,\text{m}} \left[\operatorname{erfc}\left(\sqrt{2}\frac{x_{0.1}}{a}\right) - \operatorname{erfc}\left(\sqrt{2}\frac{x_{0.9}}{a}\right) \right] \\ &+ 2\kappa_{1,\text{bf}} \left[1 - \operatorname{erfc}\left(\sqrt{2}\frac{x_{0.1}}{a}\right) \right] \end{aligned} \quad (53)$$

which we use to replace a factor $\kappa_1 \sqrt{\pi/2}$ in equation (26).

The question remains of how to rapidly find values for $\eta_{0.1}$ and $\eta_{0.9}$. Again, in the spirit of finding an easily calculable approximation, and noting that even inaccurately determining these boundaries will still improve our integral calculation, let us consider a situation where all species other than hydrogen remain fully ionized. Using standard methods, we derive

$$\mu_e = \frac{2}{1 + X(2\iota - 1)}. \quad (54)$$

Incorporating this into equation (48) along with our density profile, we can show

$$\rho_0 e^{-\eta^2} = \frac{2 m_{\text{H}}}{[1 + (2\iota - 1)X]} \frac{1 - \iota}{\iota} A(T) \quad (55)$$

which we can rearrange and solve directly for η_{ι} . We note the particularly simple form this reduces to for $\iota = 0.5$.

For similar reasons to the single zone model, we evaluate κ_{bf} and κ_{ff} at the point of highest density in their region (eg. either at $\eta_{0.9}$ or η_{max} for free-free). Given the rapid density variation in the mixed zone, we evaluate κ_{m} at $\eta_{0.5}$ or η_{max} as appropriate. The possible integration schemes are illustrated schematically in Figure 9.

4.3. Frequency Dependence $\beta_c = \beta_c(\eta, \nu)$

The parameter β_c has a direct frequency dependence from the ν^{-3} in opacity and also dependence through both κ_1 and ϵ . For regions where the Gaunt factors are slowly changing functions

of frequency eg. along the Paschen continuum in the 4000–8000 Å range or when free-free opacity is dominating, we ignore the small error introduced by neglecting the contribution of g_{ff} and g_{bf} to κ_1 . Instead we need only correct for the direct and ϵ frequency dependence of β_c . Thus,

$$\beta_c(\nu) \approx \beta_c(\nu_0) \left(\frac{\nu_0}{\nu}\right)^{\frac{6}{10-\Gamma}} \left(\frac{\epsilon}{\epsilon_0}\right)^{\frac{2}{10-\Gamma}}. \quad (56)$$

With this correction we have only to calculate β_c accurately at a single wavelength with the iterative method outlined above. The lightcurve behaviour as a function of both wavelength and time then follows immediately from the combination of (56) and (29).

4.4. Time Dependence $\beta_c = \beta_c(\eta, \nu, \beta)$

The dependence of β_c on time again comes through both κ_1 and ϵ (if $\Gamma \neq 0$). In principle, we can use a similar expression to equation (56) also to correct for the ϵ time-dependence. However, the exponential nature of the expression renders the form of the lightcurves more complex and less instructive than that derived above. As a result, this correction is probably best included only in numerical solutions. More seriously, we cannot, in general, predict the future ionization structure for a mixed composition gas from its current state. Thus, the time-dependence of κ_1 can, in general, only be included with numerical solution at a series of different times β . The exception to this rule is when we can be sure that the dominant opacity is and will remain free-free throughout the time considered. In this case κ_1 is a constant in time and we can use the same rapid approximation as the previous section.

4.5. Comparison of Integral Methods

We can lift the restriction to the purely free-free opacity case by iterative numerical solution of the Saha equations for a gas of mixed composition at each time in the lightcurve. From the ionization profile of each species we can in principle determine the opacity at any point.

We compared the results achieved by the two integration lines of sight $y = y_m$ or 0 and using 1- or 3-zone integration schemes. The total continuum opacity was calculated numerically using

using the methods of Gray (1976) with the exception of H^- bound-free (Geltman 1962) and free-free (Stilley & Callaway 1970), He^- (McDowell, Williamson & Myerscough 1966) and HeI bound-free (Huang 1948). Calculating β_c from this opacity we can iterate to a consistent solution at each time. Altering the number of zones used yielded virtually no discernable effect on the predicted lightcurves. For temperatures around 16 000 K, the two lines of sight considered produced results differing by at most around 0.5%. However, at lower temperatures the predicted fluxes could differ more, reaching around 5% at 10 000 K (see Figures 10 and 11).

5. Comparison to Observation - Deducing Fireball Parameters

The model was fitted to lightcurves for the flickering in the dwarf nova SS Cyg and the ‘bump phase’ of SN 1987A. We employed a χ^2 minimization amoeba code (Press et al. 1992) to derive the best-fit values for M , a_0 , T_0 , t_0 , H , and Γ . We use the approximation that the ionization fractions for all the species are well represented by the conditions at $x = 0, y = y_m$ and use the single zone integration approach to arrive at a self-consistent solution for β_c and κ_1 there at each time.

5.1. SS Cygni

Rapid spectroscopy of SS Cyg was carried out using the Low Resolution Imaging Spectrograph (LRIS: Oke et al. 1995) on the 10-m Keck II telescope on Mauna Kea, Hawaii, between UT 09:38 and 09:56 on 6 July 1998, covering orbital phases 0.8276 to 0.8715. The instrumental set and data reduction were the same as described by Steeghs et al. (2001), O’Brien et al. (2001) and Skidmore et al. (2003). 14,309 spectra were obtained using the rapid data acquisition system. The spectra covered 3259–7985 Å with 2.4 Å pixel⁻¹ dispersion and a mean integration time of 72.075 ms and no dead-time between individual spectra. Further details of these observations are given in Skidmore et al. (in prep). A particular flickering event was isolated between UT 9:39:10 and UT 9:43:44 and flux from other sources removed by fitting, for each wavelength, a low order polynomial to the fluxes both before and after the event. Lightcurves were formed from the mean flux in the regions 3590–

3650 Å, 4165-4270 Å, 4520-4620 Å, 5100-5800 Å, 5970-6500 Å and 7120-7550 Å at 2 s resolution.

Model lightcurves were computed using a distance of 166 pc (Harrison et al. 1999) and assuming solar composition. It appears that the disagreement is dominated by the systematic error of the oversimplicity of our model rather than observational errors. Accordingly, we carried out fits both weighting the data points according to their formal observational errors and with equal weighting. We plot the derived analytic lightcurves alongside the observations in Figures 12 and 13. From each set of derived parameters, we carried out a detailed numerical integration of the opacity calculated with an LTE ionization varying across the density profile as described in Pearson, Horne & Skidmore (2003). These models allowed us to generate a timeseries of continuum spectra and “numerical” lightcurves for comparison to the data in each case. These numerical lightcurves are also plotted in the Figures. The fitted value of Γ is close to zero in both cases and so we refitted the data fixing $\Gamma = 0$ exactly. These results are shown in Figures 14 and 15. The best-fit parameters for each case are summarised in Table 5.1.

Although we would expect the numerical lightcurves to more accurately represent reality, the analytic lightcurves generally fit the data better. This is unsurprising since the parameters used in both cases have been optimized for the analytic forms. The numerical lightcurves do seem closer to the data in the 3615 Å window in Figures 12 and 13. However, Figures 14 and 15 and our other unpublished lightcurves suggest that this is serendipitous. The difficulty in reproducing the Balmer jump may well reflect that we have 5 fitting points on the Paschen Continuum (wavelengths longer than 3646 Å) and only one above the Balmer jump. Since the continuum level will have a close to ν^{-3} relationship between discontinuities, fixing the level at several points may well bias the parameters towards an accurate fit here rather than the more complex interplay of parameters required to accurately reproduce the Balmer jump. In ideal circumstances we would like several more points at shorter wavelengths to address this issue.

The derived masses, $M \sim 1.6 \times 10^{17}$ kg are equivalent to ~ 400 s of the estimated mean mass transfer rate from the secondary of $\dot{M} \approx$

4×10^{14} kg s $^{-1}$ and $\sim 2 \times 10^{-4}$ of the total disk mass $M_{\text{disk}} \approx 7 \times 10^{20}$ kg (Schreiber & Gänsicke 2002). Similarly, the lengthscale of the expanding region, $a \sim 9.1 \times 10^6$ m is $\sim 1.5\%$ of the estimated disk radius $R_{\text{disk}} \approx 6 \times 10^8$ m (Schreiber & Gänsicke 2002). The kinetic energy is much greater than the thermal energy $E_{\text{th}} \approx 4 \times 10^{25} \left(\frac{M}{10^{17} \text{ kg}}\right) \left(\frac{T}{20\,000 \text{ K}}\right)$ J but comparable to that of a putative, moderately strong, magnetic field in a sphere of radius a_0 , $E_{\text{mag}} = 6 \times 10^{28} \left(\frac{a_0}{10^7 \text{ m}}\right)^3 \left(\frac{B}{6 \text{ T}}\right)^2$ J.

We generated full optical spectra from the ‘6-parameter weighted’ set of values and compare them to the observed spectra at three different times in Figure 16. The model data have been convolved with the instrumental blurring of 9.8 Å FWHM. The results show how parameters derived from the analytic forms for the continuum lightcurves can subsequently be used to reproduce spectra. The agreement with observation at early times is remarkable. At the peak flux and later, however, the models predict more metal and stronger lines than are observed, particularly in the 3000–5000 Å range. Many of the relative line strengths, however, are still reproduced.

5.2. SN 1987A

Given the similarities in the mechanisms underlying the flickering lightcurves in our models and those of supernovae, we attempted to fit the UBVRI photometric data for SN 1987A obtained from Catchpole et al. (1987). The data were converted to fluxes using the standard values and effective wavelengths for the bands in Murdin (2001). The fits assumed an interstellar reddening $E(B-V)=0.15$ (Hamuy et al. 1988; Fitzpatrick 1988) and assumed the same distance to the LMC of 50.1 kpc as Catchpole et al. (1987). Given the results of sophisticated NLTE spectral and lightcurve modelling (eg. Mitchell et al. 2002) we should not expect an accurate match between our simple models and the SN 1987A observations. However, it will allow us to highlight the underlying similarities of these problems and to gauge the robustness of our derived parameters. The fits used only the data after JD 2446875.0 to eliminate the flash phase and the data were all assigned equal weights. For the sake of continuity with the SS Cyg fit, we continued to allow 6 fit

Model	M	a_0	T_0	t_0	H	Γ	v_0	E_{kin}
SS Cyg	(10^{17} kg)	(10^6 m)	(10^4 K)	(UT)	(s^{-1})		(km s^{-1})	(10^{28} J)
6 param. weight.	1.6	9.8	1.91	9.6680	0.090	-0.092	890	9.7
6 param. unweight.	1.6	8.1	2.07	9.6677	0.106	-0.064	860	8.8
Isothermal weight.	1.5	7.4	2.38	9.6679	0.115	—	860	8.3
Isothermal unweight.	1.5	11.0	2.38	9.6691	0.078	—	860	8.4
SN 1987A	(10^{31} kg)	(10^{13} m)	(10^3 K)	(MJD)	(10^{-8} s^{-1})		(km s^{-1})	(10^{43} J)
5-band UVBRI	2.6	2.1	4.72	47018.7	7.2	0.066	1500	4.5
4-band BVRI	2.5	2.2	4.69	47025.3	7.0	0.071	1500	4.3

Table 1: Derived and auxiliary parameters from the analytic fits to flickering of SS Cyg and the lightcurve of SN 1987A.

Comparison of Model and Data Spectra

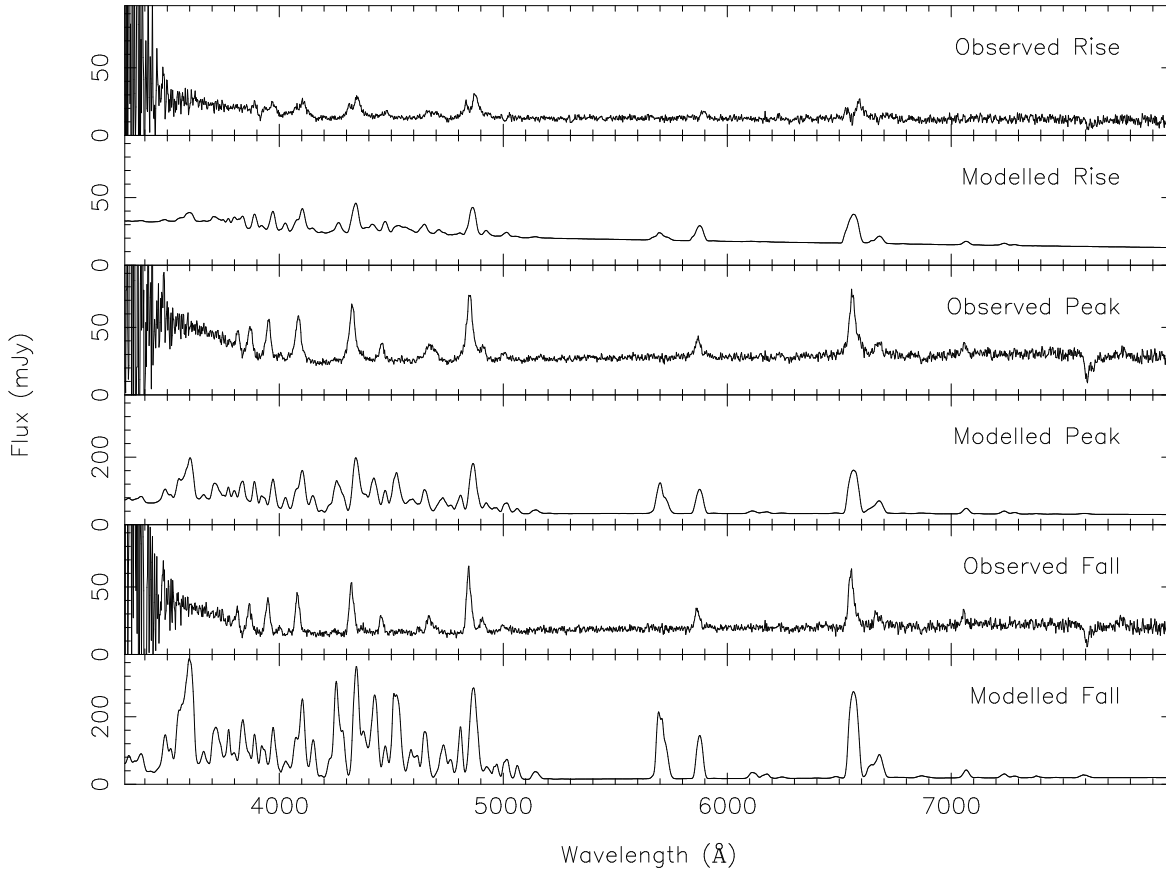


Fig. 16.— Comparison of 3 spectra at UT 9.6722 (rise), 9.6830 (peak) and 9.6916 (fall) calculated from numerical integration across our fireballs with the observed spectra of SS Cyg. The ‘6 parameter weighted’ values were used to generate the numerical spectra.

parameters rather than fixing the combination of t_0 and H to give a launch time of JD 2446849.82 when the associated neutrino event was detected by Kamiokande-II (Koshiya 1987). Since we have not attempted to remove a “background” level the fit may be contaminated by the early stages of the radioactive tail. However, the flux in this region is dominated by the expanding/collapsing photosphere effect and any heating should show up in the fitted value of Γ differing from zero.

We see in Figure 17 that we can achieve a qualitative match between the analytic expression and the data. However, the U band is particularly poorly reproduced, representing the effect of blanketing noted by Menzies et al. (1987). We refitted to the data using just the BVRI bands and show the results in Figure 18. The parameters for the fits are included in Table 5.1. We see that eliminating the U band data has relatively little effect and derive a value for the mass of the material in the expansion of $M = 2.6 \times 10^{31}$ kg ($\approx 13M_\odot$). This compares to an estimate of $7M_\odot < M_{\text{env}} < 11M_\odot$ by Saio, Nomoto & Kato (1988). The typical expansion velocity of 1500 km s^{-1} compares to a value derived from measurements of the blueshifts in P Cygni profiles of $\sim 2500 \text{ km s}^{-1}$ at maximum light (McCray 1993). Typical estimates of $E_{\text{kin}} \sim 2 \times 10^{44}$ J (Bethe & Pizzochero 1990; Woosley 1988) are somewhat larger than our $E_{\text{kin}} \approx 4 \times 10^{43}$ J.

It is unsurprising that the lightcurves do not match in detail, since the Gaussian density profile we have assumed does not accurately represent supernova ejecta. In particular, the reversal of the fast rise and slow decline derived analytically can be understood from the way in which a photosphere marching inwards through a shell (in comoving coordinates) evolves. In the shell case, the material will first become optically thin at low impact parameters once the photosphere reaches the inner surface of the shell and later at higher impact parameters with their greater path-lengths through the shell material. While these can not be considered in any sense a good fits, we do retrieve values for the mass, size and temperature (see Figure 19) for this phase comparable with those given by Catchpole et al. (1987). We also see the same isothermal behaviour from the lightcurve analysis as those authors. The size of our photosphere is less than the radius they de-

rive which is consistent with our including both optically thick and thin emission regions whereas they treat all the emission as optically thick. Our lightcurves also sometimes show an intriguing feature (unfortunately most apparent in the poorly fitted U band) of a point of inflexion at around JD 2446960. This is reminiscent, in timing and in character, of the break in the lightcurves attributed to heating by radioactive decay. In our lightcurves, however, it appears to arise from the point at which the material becomes completely optically thin with no contribution from an optically thick core region. All these factors, showing reasonable results for SN 1987A despite the inherent simplicity of our model, reinforce our confidence in the robustness of the parameters derived for SS Cyg which had much better agreement between data and theory.

6. Summary

We have derived a formalism and analytic expressions applicable to a variety of systems that reproduces the evolution of their optical lightcurves. The method has been tested for two widely different cases allows us to derive reasonable values for the physical parameters involved in the expansion. There is encouraging agreement with a method using a full integration of the opacity across the expanding region to generate both lightcurves and spectra. We have seen how the flickering of close binary systems can be modelled as smaller, hotter analogues of the well known rebrightening “bump” in supernovae lightcurves. We hope to test this approach further by comparison to data from LMXBs and other systems in the future.

We thank the referee for the thoughtful and helpful suggestions in response to an earlier version of this paper. KJP has been supported, in part, by the U.S. National Science Foundation through grant AST-9987344 and, in part, through LSU’s Center for Applied Information Technology and Learning. He also thanks Juhan Frank for stimulating discussions that improved this paper.

REFERENCES

Abramowitz M., Stegun I. A., 1972, Handbook of Mathematical Functions, Dover, New York,

- 10th Edition
- Baptista R., Bortoletto A., Harlaftis E. T., MNRAS, 335, 665
- Baptista R., Bortoletto A., ApJ, 128, 411
- Bethe H. A., Pizzochero P., 1990, ApJL, 350, 33
- Bowers R. L., Deeming T., 1984, Astrophysics I: Stars, Jones and Bartlett, Boston
- Bruch A., 1992, A&A, 266, 237
- Bruch A., 2000, A&A, 359, 998
- Catchpole R. M., Menzies J. W., Monk A. S., Wargau W. F., Pollacco D., Carter B. S., Whitelock P. A., Marang F., Laney C. D., Balona L. A., Feast M. W., Lloyd Evans T. H. H., Sekiguchi K., Laing J. D., Kilkenny D. M., Spencer Jones J., Roberts G., Cousins A. W. J., van Vuuren G., Winkler H., 1987, MNRAS, 229, 15p
- Fitzpatrick E. L., 1988, ApJ, 335, 703
- Gaunt J. A., 1930, Phil. Trans., 229, 163
- Geltman S., 1962, ApJ, 136, 935
- Gray D. F., 1976, Observations and Analysis of Stellar Photospheres, New York, Wiley
- Glasco H. P., Zirin H., 1964, ApJS, 9, 193
- Hamuy M., Suntzeff N. B., Gonzalez R., Gabriel M., 1999, AJ, 95, 63
- Harrison T. E., McNamara B. J., Szokdy P., McArthur B. E., Benedict, G. F., Klemola A. R., Gilliland R. L., 1999, ApJ, 515, L93
- Hawley J. E., Babluis S. A., 1991, ApJ, 376, 223
- Honey W. B., Bath G. T., Charles P. A., Whitehurst R., Jones D. H. P., Echevarria J., Arevalo M. J., Solheim J.-E., Tovmassian G., Takagishi K., 1989, MNRAS, 236, 727
- Huang S., 1948, ApJ, 108, 354
- Jeffreys H., Jeffreys B. S., 1956, Methods of Mathematical Physics, Cambridge Univ. Press, Cambridge, 3rd Edition
- Keady J. J., Kilcrease D. P., 2000, in, Cox A. N., Allen's Astrophysical Quantities, Chapter 5, Springer Verlag, New York, 4th Edition
- Koshiba M., 1987, IAU Circ. No. 4338
- Lang K. R., 1980, Astrophysical Formulae, Springer Verlag, New York, 2nd Edition
- McCray R., 1993, ARA&A, 31, 175
- McDowell M. R. C., Williamson J. H., Myerscough V. P., 1966, ApJ, 144, 827
- Mauche C. W., Robinson E. L., 2001, ApJ, 562, 508
- Menzies J. W., Catchpole R. M., van Vuuren G., Winkler H., Laney C. D., Whitelock P. A., Cousins A. W. J., Carter B. S., Marang F., Lloyd Evans T. H. H., Roberts G., Kilkenny D., Spencer Jones J., Sekiguchi K., Fairall A. P., Wolstencroft R. D., 1987, MNRAS, 227, 39p
- Mitchell R. C., Baron E., Branch D., Hauschildt P. H., Nugent P. E., Lunqvist P., Blinnikov S., Pun C. S. J., 2002, ApJ, 574, 293
- Murdin P., 2001, Encyclopedia of Astronomy and Astrophysics, IOP Publishing Ltd. and Nature Publishing Group, London
- O'Brien K., Horne K., Boronson B., Still M., Gomer R., Oke J. B., Boyd P., Vrtilik S. D., 2001, MNRAS, 323, 484
- Oke J. B., Cohen J. G., Carr M., Cromer J., Dinigizian A., Harris F. H., Labrecque S., Lucinio R., Schall W., Epps H., Miller J., 1995, PASP, 107, 375
- Patterson J., 1981, ApJS, 45, 517
- Pearson K. J., Horne K. D., Skidmore W., 2003, MNRAS, 388, 1067
- Press W. H., Teukolsky S. A., Vetterling W. T., Flannery B. P., 1992, Numerical Recipes in Fortran, Cambridge Univ. Press, Cambridge, 2nd Edition
- Ritter H., Kolb U., 2003, A&A, 404 301
- Saio H., Nomoto K., Kato M., 1988, Nature, 334, 508
- Schreiber M. R., Gänsicke B. T., 2002, A&A, 382, 124

Skidmore W., O'Brien K., Horne K., Gomer R.,
Oke J. B., Pearson K. J., 2003, MNRAS, 338,
1057

Skidmore W., O'Brien K., Pearson K. J., Horne
K., Gomer R., Oke J. B., in prep.

Steeeghs D., O'Brien K., Horne K., Gomer R., Oke
J. B., 2001, MNRAS, 323, 484

Stilley J. L., Callaway J., 1970, ApJ, 160, 245

van Teeseling A., 1997, A&A, 324, L73

Warner B., 1995, Cataclysmic Variable Stars,
Cambridge Univ. Press, Cambridge

Warner B., 2004, PASP, 116, 115

Wells L. D., 1896, Harv. Coll. Obs. Circ., No. 12

Welsh W. F., Wood J. H., 1995, in IAU Colloq.
151, Flares and Flashes, ed. J. Greiner, H. W.
Duerbeck, R. E. Gershberg (Lecture Notes in
Physics, 454), Springer, Berlin, 300

Woosley S. E., 1988, ApJ, 330, 218

Wynn G. A., King A. R., Horne K. D., 1997, MN-
RAS, 286, 436

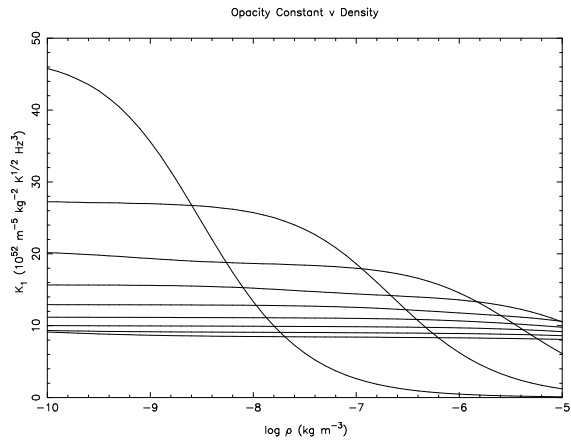


Fig. 8.— The value of κ_1 at 5000 \AA for temperatures ranging in 2000 K steps from 8000 K (upper left curve) to $24\,000 \text{ K}$.

This 2-column preprint was prepared with the AAS L^AT_EX
macros v5.2.

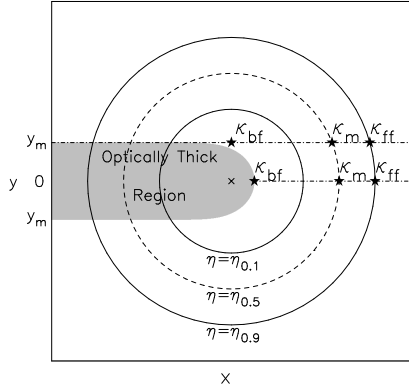


Fig. 9.— Schematic representation of the alternative integration schemes. The dot-dashed lines mark the two possible lines of sight considered for an observer (at $x = \infty$). Along the $y = 0$ line of sight the one-zone model would calculate β_c using $\kappa (= \kappa_{bf})$ evaluated at the photosphere. For a three zone scheme β_c would be calculated using a combination of the relevant opacities evaluated at the indicated positions. The boundaries for each zone occur at the intersection of the dot-dashed line with the solid lines. Similarly the position where the opacities would be calculated for an optically thick/thin transition line of sight are indicated. While the circles of η_ν have been placed purely for illustrative convenience, the position of the photosphere has been calculated assuming $\tau_0 = 10$. Other possible combination exist depending on the relative positions of the photosphere, peak density and ionization boundaries.

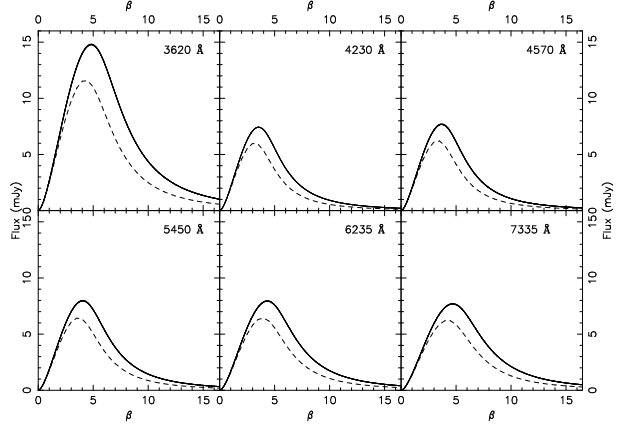


Fig. 10.— Comparison of predicted lightcurves using the 4 combinations of 1- or 3-zone and $y = 0$ or y_m line of sight integration methods. The 4 methods produce virtually indistinguishable results. The parameters of the model are $M = 3.0 \times 10^{16}$ kg, $a_0 = 7.5 \times 10^6$ m, $T_0 = 16\,000$ K and $\Gamma = 0$. A lightcurve calculated from a full numerical integration of the opacity through the fireball is plotted as a dashed line. A distance of 166 pc has been assumed.

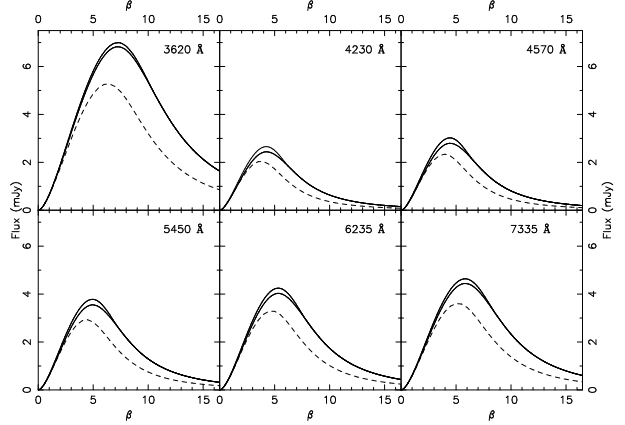


Fig. 11.— The same comparison as Figure 10 but with $T_0 = 10\,000$ K. The 1- and 3- zone models are indistinguishable in either case. The $y = 0$ models produce slightly lower peak fluxes.

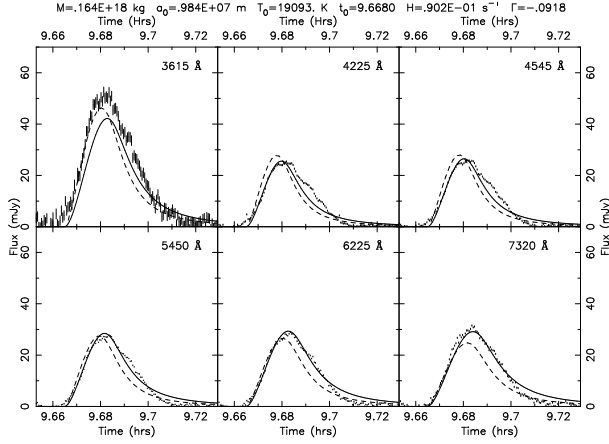


Fig. 12.— Analytic fits (solid) to the SS Cyg data points and lightcurves generated from numerically calculated spectra using the best-fit parameters (dashed). Γ was allowed to be a fit parameter and the points were weighted according to the observational errors.

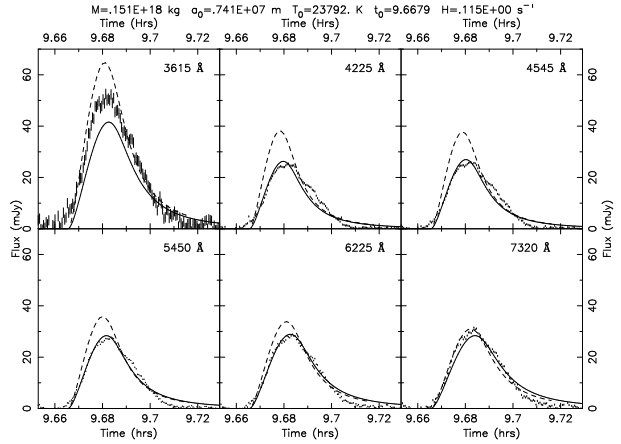


Fig. 14.— Same comparison as Figure 12, $\Gamma = 0$ (isothermal) was fixed and the points were weighted according to the observational errors.

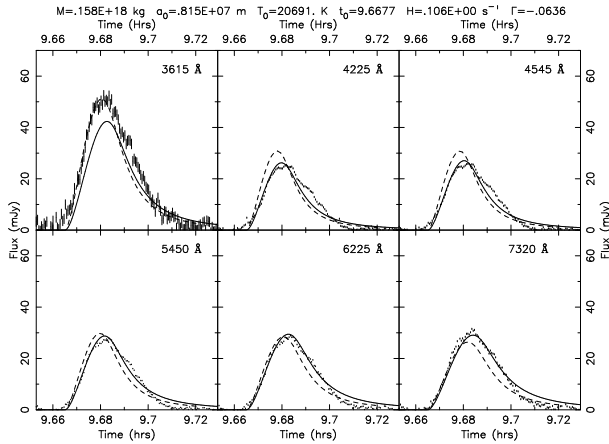


Fig. 13.— Same comparison as Figure 12, Γ was allowed to be a fit parameter and the points were weighted equally.

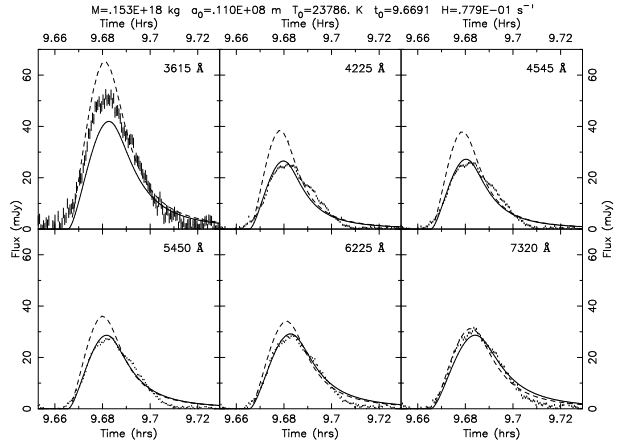


Fig. 15.— Same comparison as Figure 12, $\Gamma = 0$ (isothermal) was fixed and the points were weighted equally.

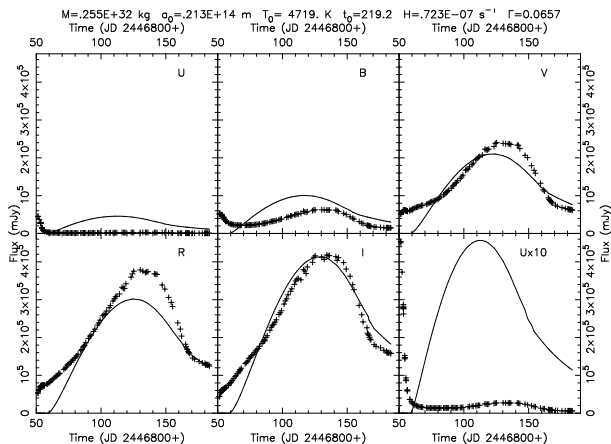


Fig. 17.— Analytic fits (solid) to the UBVR I SN 1987A data of Catchpole et al. (1987). Γ was allowed to be a fit parameter and all the datapoints with $t > \text{JD } 2446875.0$ were given equal weight.

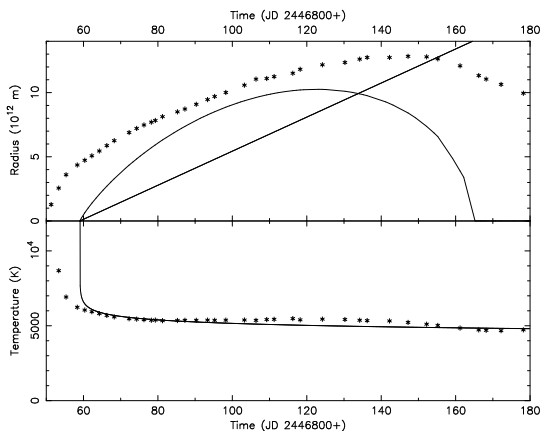


Fig. 19.— The temperature and radius derived by Catchpole et al. (1987) (asterisks) and temperature, optically thick radius (in the V band) and current lengthscale from our UBVR I fit parameters.

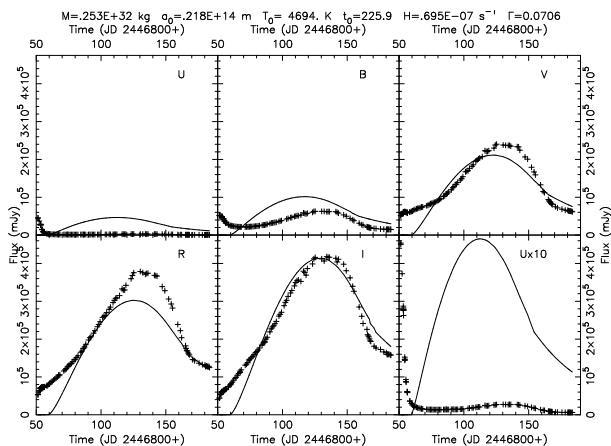


Fig. 18.— Same comparison as Figure 17 fitting only BVRI band data.